ISSN 1361-8415 (c) 2006 Elsevier

Plaque Development, Vessel Curvature, and Wall Shear Stress in Coronary Arteries assessed by X-ray Angiography and Intravascular Ultrasound

Andreas Wahle [a,*], John J. Lopez [d], Mark E. Olszewski [a], Sarah C. Vigmostad [b], Krishnan B. Chandran [b], James D. Rossen [c], and Milan Sonka [a]

[a] *The University of Iowa, Electrical and Computer Engineering*

[b] *The University of Iowa, Biomedical Engineering*

[c] *The University of Iowa, Internal Medicine*

[d] *The University of Chicago, Medicine, Division of Cardiology*

Abstract

The relationships among vascular geometry, hemodynamics, and plaque development in the coronary arteries are complex and not yet well understood. This paper reports a methodology for the quantitative analysis of in-vivo coronary morphology and hemodynamics, with particular emphasis placed on the critical issues of image segmentation and the automated classification of disease severity. We were motivated by the observation that plaque more often developed at the inner curvature of a vessel, presumably due to the relatively lower wall shear stress at these locations. The presented studies are based on our validated methodology for the three-dimensional fusion of intravascular ultrasound (IVUS) and x-ray angiography, introducing a novel approach for IVUS segmentation that incorporates a robust, knowledge-based cost function and a fully optimal, three-dimensional segmentation algorithm. Our first study shows that circumferential plaque distribution depends on local vessel curvature in the majority of vessels. The second study analyzes the correlation between plaque distribution and wall shear stress in a set of 48 in-vivo vessel segments. The results were conclusive for both studies, with a stronger correlation of circumferential plaque thickness with local curvature than with wall shear stress. The inverse relationship between local wall shear stress and plaque thickness was significantly more pronounced ($p<0.025$) in vessel cross sections exhibiting compensatory enlargement (positive remodeling) without luminal narrowing than when the full spectrum of disease severity was considered. The inverse relationship was no longer observed in vessels where less than 35% of vessel cross sections remained without luminal narrowing. The findings of this study confirm, in-vivo, the hypothesis that relatively lower wall shear stress is associated with early plaque development.

Key words: Coronary Atherosclerosis, Plaque Distribution, Morphology, Hemodynamics, Data Fusion, X-ray Angiography, Intravascular Ultrasound

* 3320 Seamans Center for Engineering, Iowa City, IA 52242, U.S.A.
Email address: andreas-wahle@uiowa.edu (Andreas Wahle).
URL: http://www.engineering.uiowa.edu/∼awahle (Andreas Wahle).

1 Introduction

Coronary atherosclerosis starts early in life and is a major cause of death in industrialized countries. Therefore, the study of plaque development and progression is of high interest. An early stage of plaque development is intimal thickening (Stary et al., 1994, 1995); however, the lumen size is preserved during the early atherosclerotic process due to *compensatory enlargement*. Figures 1(a)–(c) illustrate this process. Glagov et al. determined that luminal narrowing (stenosis) generally occurs after the plaque area exceeds about 40% of the cross-sectional vessel area (Glagov et al., 1987). Obstructive stenoses are most frequently treated by percutaneous transluminal coronary angioplasty (PTCA) and subsequent stenting to restore the lumen, as illustrated in Figure 1(d).

Despite the routine nature of coronary interventions, understanding the mechanisms of plaque development in coronary arteries and the roles of hemodynamics and vessel geometry is of utmost importance for predicting areas of future plaque development, and possible future clinical events. Previous studies have linked plaque development with low wall shear stress (Gibson et al., 1993), which in turn depends on the vessel geometry. Friedman et al. (1987) have reported that the intima was generally thicker at sites exposed to lower wall shear stresses in a coronary artery branch. Ideally, the wall shear stress distribution at the onset of atherosclerosis should be analyzed and then related with subsequent plaque progression. In vessel segments with initially low wall shear stress one would expect larger plaque accumulation; however, there are only a limited number of longitudinal studies that have compared plaque distribution in relation to local wall shear stress distribution at multiple points in time. While Wentzel et al. (2003a) used a relatively short interval of six weeks to follow-up, Stone et al. (2003) compared distributions in wall shear stress and plaque development over a period of six months.

Selective x-ray angiography has been the method of choice for diagnostic and interventional cardiology for decades, but using angiography alone allows only a limited analysis of the vessel lumen by quantitative coronary angiography (Brown et al., 1991; Reiber et al., 2000). Similarly, three-dimensional (3-D) analyses from biplane angiography can only offer elliptical approximations of the lumen shape (Wahle et al., 1995). Although attempts to achieve further refinement of the lumen shape based on x-ray densitometry have shown to be successful in larger structures [e.g., iliac arteries (Pellot et al., 1994) or ventricles (Prause and Onnasch, 1996)] and also in coronary arteries (Reiber et al., 1982; Bao et al., 1990), x-ray angiography cannot directly depict plaque distribution or composition. Instead, these are approximated indirectly from the contrast-filled lumen (Seiler et al., 1992; Wahle et al., 1995). Substantially more detailed cross-sectional information can be obtained by intravascular ultrasound (IVUS), an established complement to x-ray angiography (von Birgelen et al., 1997). An example of an IVUS frame is shown in Figure 1(e). Most importantly, IVUS allows the accurate assessment of plaque distribution and volume, as well as the effect

of interventional treatment of coronary stenosis on plaque and vessel morphology (Reiber et al., 2000). In contrast to x-ray angiography, compensatory enlargement is directly visible in IVUS. The most challenging task is the determination of the lumen/plaque and media/adventitia borders in IVUS while limiting the need for user interaction at the same time. Existing methods (Herrington et al., 1992; Li et al., 1994; Sonka et al., 1995b; Klingensmith et al., 2000; Brusseau et al., 2004) use a variety of segmentation algorithms, but achieve only limited success. The limitations of these approaches are mainly due to the lack of higher-dimensional context, or the lack of knowledge-based segmentation criteria. Our paper therefore expands on this important issue and presents a new 3-D graph-theoretic approach. Recent developments in IVUS technology also allow plaque classification (Nair et al., 2002).

In this in-vivo 3-D IVUS study, we aim to verify in a cohort of patients the hypothesis that regions of relatively lower initial wall shear stress show a relatively higher plaque accumulation. As is typical for in-vivo coronary IVUS studies, all subjects imaged had cardiac catheterization, since IVUS is not clinically indicated in patients with limited or no significant obstructive coronary atherosclerosis. Consequently, the enrolled subjects invariably exhibited advanced atherosclerosis, thus the relationships we observed were between a substantially altered coronary morphology and the related hemodynamic shear stress conditions. It has been shown that, with extensive luminal narrowing, the inverse relationship between plaque thickness and wall shear stress is no longer preserved (Wentzel et al., 2003b). Thus, we have developed a methodology that automatically categorizes vessel segments by disease severity and allows indirect verification of the hypothesis by exclusion of segments at later disease stages, to attempt to overcome the limitations of one-time imaging of patients with advanced atherosclerotic coronary disease.

In contrast to wall shear stress, vascular (not luminal) curvature is not substantially changed by atherosclerosis and thus can serve as a surrogate of the pre-atherosclerotic hemodynamic conditions. Therefore, the relationship between vessel curvature and plaque distribution was studied in addition to the relationship between wall shear stress and plaque distribution.

2 Methods

The following subsections describe the generation of the spatial and spatio-temporal models of coronary arteries based on our previously presented fusion methodology (Section 2.1), with special emphasis on more recent developments in the field of IVUS segmentation (Section 2.3). Angiographic segmentation (Section 2.2) and the creation of the 3-D/4-D models (Section 2.4) are only briefly addressed since they are explained in more detail elsewhere. The remaining sections provide details on the morphologic and hemodynamic quantitative indices (Section 2.5), and the classification of circumferential plaque distribution with respect to those indices (Section 2.6). These

indices and classifications are then utilized for the in-vivo patient studies presented in Section 3.

2.1 Multi-Modality Fusion of X-ray Angiography and Intravascular Ultrasound

We have developed a comprehensive system that generates geometrically correct 3-D and/or 4-D (i.e., 3-D plus time) reconstructions of coronary arteries and computes quantitative indices of coronary lumen and wall morphology. The reconstructions serve as input for hemodynamic analyses and allow for interactive visualization (Wahle et al., 1999; Reiber et al., 2000; Olszewski et al., 2003; Wahle and Sonka, 2005). A flowchart outlining the system is given in Figure 2. In general, vessel curvature and torsion are derived from biplane (or a pair of single-plane) x-ray angiograms, and the cross-sectional information is obtained from IVUS. Thus, the resulting model accurately reflects the spatial geometry of the vessel and includes any accumulated plaque. The angiography and IVUS data are retrospectively ECG-gated and segmented. In order to obtain a 4-D model as a set of 3-D models (one per phase), angiographic and IVUS data corresponding to the end diastole form the phase #0; using constant offsets (in $\%R-R$ or in milliseconds from phase #0), further phases are extracted (Wahle et al., 2001). Fusion leads to the 3-D/4-D *plain model*, consisting of the lumen/plaque and media/adventitia contours oriented relative to the IVUS catheter. After tetrahedral meshing, this model is suitable for hemodynamic analyses. Morphologic analyses are performed following resampling of the cross sections orthogonal to the vessel centerline, to eliminate distortions from the position of the IVUS catheter within the vessel. The quantitative results *annotate* the resampled contour model, which is then used for visualization and further analyses. Our system utilizes conventional PC hardware and widely available software tools. Standardized storage formats for parameters and contours have been adopted to ensure proper interfacing between our fusion system and commercially available analysis software packages, and to enhance data sharing and collaboration (Olszewski et al., 2003).

2.2 Segmentation of Angiographic Data

Segmentation of angiographic images has a long history and is well established in quantitative coronary analysis. Examples of such software include Brown et al. (1977), Kirkeeide et al. (1982), and Beier et al. (1991). A methodological overview can be found in Reiber et al. (2000). All of these methods aim for identifying the vessel lumen borders as visible in the angiograms. The approach of Sonka et al. (1995a) determines both borders simultaneously as a single path through the graph; van der Zwet and Reiber (1994) developed an approach to segment difficult border shapes.

For the purpose of fusion between angiography and IVUS, the angiographic lumen borders are only utilized to establish a reference for the absolute orientation of the

IVUS data in 3-D space. Consequently, requirements for the accuracy of the border segmentation can be reduced, and a dynamic programming approach with edge-based cost functions was employed. In addition to the lumen outline, also the IVUS catheter needs to be segmented to establish its 3-D path. Therefore, a third cost function was used that models a gray-value ridge within the lumen and also separates the search space for the two borders as an additional constraint. For segmentation, the user only has to identify the location of the IVUS transducer, shown in its distal position since the angiograms were taken before the pullback started; the proximal endpoint, usually the ostium; and a few intermediate points to create a spline, which defines the region of interest for the graph search with a selectable width.

2.3 Segmentation of IVUS Image Data

Due to the challenges inherent to the images, one of the important areas of research is the segmentation of the IVUS data. A comprehensive review article on IVUS segmentation and quantitative evaluation has been presented by Klingensmith et al. (2003). Approaches to identify the lumen/plaque and media/adventitia borders include those based on graph search (Sonka et al., 1995b) or simulated annealing (Herrington et al., 1992). Another frequently met approach is the use of active contours *(snakes)*, which iteratively determine the borders based on energy functions (Kass et al., 1988; Klingensmith et al., 2000). Also, texture information can be taken into account. In this case, interfaces between regions are searched for rather than explicit edges (Mojsilović et al., 1997; Zhang et al., 1998).

It is well known that IVUS images contain artifacts from various sources, thus requiring the design of cost functions that incorporate a-priori knowledge of regional and border properties to robustly and accurately identify borders. We have developed a novel approach to IVUS segmentation, which combines 3-D optimum graph search with a three-tiered cost function. Since a 3-D fusion model is not available at the time the IVUS data are segmented, they are initially treated as a stack of 2-D images forming a 3-D volume. While many approaches, e.g., the segmentation method of Li et al. (1994), perform an initial longitudinal segmentation over the entire pullback to establish the 3-D context, followed by cross-sectional contour detection, our algorithm operates in a true 3-D manner. Truly 3-D IVUS segmentations were thus far limited to active surfaces (Klingensmith et al., 2000).

2.3.1 Graph-Based IVUS Segmentation

Prior to segmenting the IVUS image data for the lumen/plaque and media/adventitia borders, several preprocessing steps occur. The stack of IVUS images is automatically centered to account for image shifts during digitization, the field of view is identified, and the region containing the catheter is excluded from further analysis, using an

implementation of the Hough Transform. Also, stationary image components that may contain a gain offset or stationary artifacts such as the catheter ring-down are removed by subtracting the average pullback frame from each image in the pullback. The average frame is computed on a pixelwise basis over the entire pullback length, and the introduction of artifacts is avoided by limiting the results of the subtraction to a value of zero. The removal of stationary components serves as a normalization step for the learning process described in the next section, and removes any biases that may corrupt the statistical analyses also described below. The final step before beginning processing is to "unfold" the IVUS pullback so that the cylindrical surface detection problem is reformatted into an elevation map detection problem. This process is shown in Figure 3.

A method for efficient detection of the *globally optimal* surfaces representing object boundaries in volumetric datasets was recently developed by our research group (Li et al., 2004a,b). The method is capable of simultaneously detecting multiple interacting surfaces, in which the optimality is not only controlled by the cost functions designed for individual surfaces, but also confined by several geometric constraints defining the surface smoothness and interrelations. The method solves the surface detection problems by transforming the detection problem into computing minimum $s-t$ cuts in the derived geometric hypergraphs. The proposed algorithm has polynomial complexity, is computationally efficient, and allows simultaneous segmentation of the lumen/plaque and media/adventitia surfaces in the 3-D IVUS data. Consequently, the spatial and temporal contextual information is incorporated in a single optimization process yielding a pair of interacting surfaces in 3-D. This utilization of higher-dimensional knowledge, combined with the geometric constraints, allows the method to determine the optimal path in cases of vessel branchpoints, shadowing, rotational distortions, and vessel rupture. In instances where severe gaps occur, the algorithm will find the shortest path (surface) across the gap.

To further improve the efficiency of the algorithm and its robustness to noise and artifact, the automated system uses the optimal surface detection technique in a multiresolution approach. This is achieved by finding the optimal lumen/plaque and media/adventitia borders in a three-tiered sequence starting at a low resolution and continuing to a high resolution. At each resolution stage, the searched area of the graph is reduced so that more efficient use of computation time is made.

2.3.2 Cost Function Design

The cost functions used for the identification of the lumen/plaque and media/adventitia surfaces are of paramount importance for the success of the segmentation. The cost function contains three classes of information at both global and local levels: expected border properties, information theoretic criteria based on the statistical properties of ultrasound, and regional homogeneity properties. By combining these three types of information in an optimal manner, the overall segmentation process is able to over-

come common variation and artifacts of IVUS imaging. These classes are realized as a combination of the following terms:

(1) Intensity patterns learned from example;
(2) Rayleigh distribution models of ultrasound image data (Burckhardt, 1978; Wagner et al., 1983; Brusseau et al., 2004);
(3) Object homogeneity properties (Chan and Vese, 2001).

Multiresolution methods (Liang et al., 2000) and methods that attempt to integrate edge and region information (Chakraborty et al., 1996) have proven to be successful in the past. The combination of local and global features of this cost function will seek to minimize the drawbacks associated with previous techniques that concentrated on only one level; the combination of analytical and learned terms will allow the system to learn the properties of features that are not easily expressed analytically, while retaining analytical terms to help when a particular feature has not yet been seen by the system.

2.3.3 Learned Border Patterns

It has been observed that although noise, speckle, and artifacts tended to confuse previous automated methods, human tracers are still able to correctly segment the vast majority of IVUS images. This observation motivated the design of a cost function that consists of terms that are learned from experience, in addition to those that are derived analytically from the data being analyzed.

Over time, there has been an accumulation of both manually traced IVUS data sets and IVUS data sets that have been semi-automatically segmented with manual corrections. These data sets were used in the development of a cost function to learn what pixels the human observer most often chooses for border pixels. In order to perform the learning step, a window is passed over the training images. Within the window, the pattern of pixels is examined. For each pattern that contains a border pixel, the system increments an accumulator entry corresponding to that border pattern, as shown in Figure 4 for a 2-D case. An accumulator entry exists for every possible pattern, following normalization and quantization to allow for image variation and memory conservation, respectively. The accumulator can now be considered to contain the likelihood of each pattern being a border pattern.

After this training stage is complete, the learned information can be used to score an image that is to be analyzed. In the same way that the accumulator was created in the training step, patterns are examined in the image. Then, a cost image is generated by assigning a likelihood value to the pixel located at (x, y, z) based on the value found in the accumulator for the same pattern, as illustrated in Figure 5 for a 2-D case. This process results in a cost value $C_{learnedLumen}(x, y, z)$ for the lumen/plaque and $C_{learnedAdventitia}(x, y, z)$ for the medial/adventitial borders. The learned border properties may also be updated continually as the system is in use, thereby permitting

the system to gain knowledge over time and get better over time.

2.3.4 Statistical Properties of Ultrasound

It has been known for some time that the developed speckle in ultrasonic images is characterized by a Rayleigh distribution, given by: (Burckhardt, 1978; Wagner et al., 1983)

$$P(A_i) = \frac{A_i}{\alpha^2} \exp\left(-\frac{A_i^2}{2\alpha^2}\right) \tag{1}$$

where $P(A_i)$ represents the probability that pixel i has intensity A_i, and the distribution is governed by parameter α.

Recently, this knowledge has been used in the accurate segmentation of the luminal boundary in IVUS images by deformable contours that separate two regions (lumen and vessel wall) based on their global statistical properties (Brusseau et al., 2004). To adapt this concept to our optimal 3-D graph approach, the objective function for the contour estimation was approximated to produce a voxel cost at the polar-transformed image location $I(x, y, z)$ as shown in Figure 3(b), which is expressed as:

$$C_{Rayleigh}(x, y, z) = -z \ln(\hat{\alpha}_1^2) - (Z - z) \ln(\hat{\alpha}_2^2) \tag{2}$$

where Z is the height of the polar-transformed image and the parameters $\hat{\alpha}_1$ and $\hat{\alpha}_2$ are approximated as:

$$\hat{\alpha}_1 = \sqrt{\frac{1}{2z} \sum_{z'=0}^{z' \leq z} I(x, y, z')^2} \tag{3}$$

$$\hat{\alpha}_2 = \sqrt{\frac{1}{2(Z - z)} \sum_{z'=z+1}^{z' < Z} I(x, y, z')^2} \tag{4}$$

2.3.5 Region Homogeneity

Degradations in image quality due to severe vascular disease, videotape recording artifacts, or non-uniform rotational distortion can alter the development of a true Rayleigh distribution in the image speckle. Therefore, we chose to add a version of the Chan-Vese minimum variance criterion (Chan and Vese, 2001) as a third component of our cost function. This term allows segmentation without the presence of gradients,

and without the assumption of a particular statistical model. As with the Rayleigh cost term, the Chan-Vese functional is restated so that it produces a voxel cost:

$$C_{CV}(x,y,z) = \sum_{z'=0}^{z' \leq z} \left(I(x,y,z') - a_1\right)^2 + \sum_{z'=z+1}^{z' < Z} \left(I(x,y,z') - a_2\right)^2 \tag{5}$$

where a_1 and a_2 are approximated as the means of $I(\mathbf{x},\mathbf{y},\mathbf{z}_1)$ and $I(\mathbf{x},\mathbf{y},\mathbf{z}_2)$, which are sets containing all voxels below ($\mathbf{z}_1 = \{z' | 0 \leq z' \leq z\}$) and above ($\mathbf{z}_2 = \{z' | z < z' < Z\}$) the surface, respectively.

2.3.6 Combination of Cost Terms

The developed cost terms are combined into a total cost function in a pseudo-probabilistic manner such that the final segmentation produces a result that is optimal with regards to all of the terms. Prior to combination, the terms are each normalized so that they fall in the range $0 \leq C_i \leq 1$, where C_i represents any cost term. Normalization of each term is performed on a pixelwise basis with respect to the maximum of each term. In this manner, each term can be thought of as the likelihood that a certain voxel exhibits the feature that the term represents. Then, the term that jointly estimates the combination of cost terms can be represented as the product of the individual normalized terms. The learned terms and the Rayleigh separation term must be inverted in order to search for the minimum cost path, since they are maximal at the probable border locations. Also, since an additive procedure is used in the optimization, the logarithm of the product is taken at each voxel so that when the optimal surfaces are detected, it ensures that each surface optimally maximizes the joint likelihood of the cost terms over each surface. Note that $\log(\prod_{i=1}^{n} C_i) \leq 0$ for $0 < C_i \leq 1$, and minimizing a cost $\log(C)$ will also minimize C. The Rayleigh separation term is omitted from the cost of the adventitial surface because it is only well defined for a single separation point.

The total costs $C_{totalLumen}(x,y,z)$ for the lumen/plaque and $C_{totalAdventitia}(x,y,z)$ for the media/adventitia borders are then expressed as:

$$\begin{aligned} C_{totalLumen}(x,y,z) = \log\big((1 - \|C_{learnedLumen}(x,y,z)\|) \\ \bullet(1 - \|C_{Rayleigh}(x,y,z)\|) \\ \bullet \|C_{CV}(x,y,z)\|\big) \end{aligned} \tag{6}$$

$$\begin{aligned} C_{totalAdventitia}(x,y,z) = \log\big((1 - \|C_{learnedAdventitia}(x,y,z)\|) \\ \bullet \|C_{CV}(x,y,z)\|\big) \end{aligned} \tag{7}$$

2.4 Fusion of the Image Data

After the angiographic and IVUS data are segmented, *fusion* can be performed to yield a 3-D model (or a set of 3-D models in the 4-D case) for the artery. Since our fusion methodology has been described in detail elsewhere (Wahle et al., 1999; Wahle and Sonka, 2005), only a brief summary will be given here. A number of fusion systems were introduced in the late 1990's, which follow similar schemes. The catheter path is extracted from the biplane angiograms, reconstructed into 3-D space, and then used to map the IVUS images to their locations. The fusion problem is two-fold: first, the *localization* of the individual IVUS frames in 3-D; second, the estimation of the spatial *orientation* of each frame.

Some fusion systems require constant angiographic supervision of the catheter during pullback to reconstruct the respective position of the IVUS frame from the projections of the transducer (Evans et al., 1996; Pellot et al., 1996; Shekhar et al., 1996). Instead, just a single pair of angiograms, depicting the IVUS catheter in its most distal location, suffices to reconstruct the pullback path in 3-D and then follow it during the pullback (Laban et al., 1995; Prause et al., 1996). This results in reduced radiation exposure and is applicable as long as the pullback path is sufficiently stable (e.g., sheathed catheter types). Spatial reconstruction of the catheter path is performed based on the known imaging geometry and the angiographic segmentation based on the epipolar constraint. In our approach, the method described in Wahle et al. (1995) is used.

The estimation of the absolute orientation of the IVUS frames in 3-D is another critical issue and is usually resolved using the angiographic lumen as a reference. The outline of the vessel lumen is visible in both angiographic projections when a small amount of contrast dye is injected. This is utilized to establish the orientation of the IVUS frames by finding their best fit with the angiographic outline. The iterative methods of Pellot et al. (1996) and Shekhar et al. (1996) both used a local match of each individual IVUS frame with the angiographic lumen outline. In contrast to determining the orientation individually for each frame, constraints from the Frenet-Serret formulas can be used to determine the axial twist between the frames. Laban et al. (1995) implemented the Frenet-Serret formulas directly, using a Fourier parameterization to approximate the catheter path. This parameterization satisfied the requirement of a third-order derivative as implied by the rules. Our method is based on the sequential triangulation by Prause et al. (1996), employing a discrete implementation of the Frenet-Serret formulas.

Using differential geometry, only the *relative* orientation changes from frame to frame can be establish, the *absolute* orientation of the frame set yet needs to be determined. Instead of projecting the IVUS lumen onto the angiograms in order to compare it against the 2-D angiographic outline, our method goes the opposite way. A 3-D elliptical lumen outline is reconstructed from the angiograms and compared with the

IVUS lumen outline, mapped into 3-D using an arbitrary initial orientation. This allows a non-iterative approach in which a single correction angle is calculated from an initial orientation and then applied to the entire frame set (Wahle et al., 1999; Wahle and Sonka, 2005). To account for locations of ambiguous information (e.g., uniform or non-uniform rotations caused by friction of the catheter), a reliability weight is defined for each frame location, limiting its impact on the overall calculation.

2.5 Morphologic and Hemodynamic Indices

After the segmentation has been performed and the resulting set of 2-D contours has been fused with the angiographic information, a 3-D model of the vessel is obtained. From this model, morphologic and hemodynamic quantitative indices are derived. The reconstructed vascular model provides 3-D locations for 720 circumferential vertices on both lumen/plaque and media/adventitia contours, oriented with respect to the IVUS catheter path. To limit the impact of noise and possible local distortions of the contours, they are downsampled to 72 circumferential vertices each (5° wedges).

It has to be kept in mind that the IVUS catheter (and thus the center of the IVUS image) does not necessarily coincide with the vessel centerline. In fact, this out-of-center position is utilized during the fusion process to establish the absolute orientation of each IVUS frame (Wahle et al., 1999). Also, the IVUS frame is usually oriented non-parallel to the vessel course, thus requiring a resampling of the contours on a plane orthogonal to the vessel. The question remains whether to reorient the contours with respect to the media/adventitia or the lumen/plaque border. To avoid any overlap of the reorientation planes in the plaque area, the outer contour has to be used. Thus, we are determining the quantitative indices with the contours oriented perpendicularly to the vessel centerline, whereas any radius or plaque-thickness calculations are performed relative to the lumen centerline.

Therefore, we first determine the vessel centerline (i.e., based on the media/adventitia border) and then determine intermediate contour points in the longitudinal direction using cubic B-splines. Finally, all contours are reoriented to lie in a plane perpendicular to the vessel centerline. After this perpendicular resampling, the lumen centerline is determined (i.e., based on the lumen/plaque border) as a reference for subsequent morphologic analyses. This allows for the determination of the plaque thickness at each location, as well as volumetric measurements over any given subsegment of the vessel, without the distorting effects of the individual location and orientation of the IVUS catheter (Medina et al., 2003).

2.5.1 Definition of the Curvature Index

In order to determine local curvature magnitude and direction, computational geometry is employed. To distinguish between locations of “inner” vs. “outer” curvature on

the circumference of the vessel, a new scheme is introduced that weights the curvature magnitude by an index of the circumferential position of each element (Wahle et al., 2004). This *local* index is not to be confused with the overall curvature of a vessel or a vessel segment as a *global* measure.

The definition of a local curvature index consists of two steps: (1) determining the local curvature at each frame; (2) determining the curvature indices for each circumferential point within that frame. Differential geometry provides a set of three orthonormal unit vectors [Frenet frame (Wahle et al., 1999)] for each point on a curved line: $\vec{t}$ (tangent); $\vec{n}$ (normal); and $\vec{b}$ (binormal). The curvature $\kappa(s)$ is the angular velocity of the tangent $\vec{t}(s)$ at a location s of the centerline c. As shown in Figure 6(a), the normal vector $\vec{n}(s)$ always points towards the origin of the radius of curvature, thus indicating the inner curvature on the circumference. Complementarily, $\kappa(s)$ is a measure of the magnitude of the curvature.

To combine the magnitude and direction of the curvature, thereby differentiating between inner and outer curvature, we defined the scalar *curvature index* $\kappa_{\text{idx}}(s,i)$ for each point i at the frame location s as shown in Figure 6(b). A positive $\kappa_{\text{idx}}(s,i)$ indicates inner curvature, a negative index outer curvature, and an index close to zero applies for points on the sides of the curved vessel segment, i.e., perpendicular to $\vec{n}(s)$. The maximum (most positive) curvature index and the minimum (most negative) curvature index depend directly on the magnitude of the curvature $\kappa(s)$ for that frame.

The circumferential position of the vertex point indicating the inner curvature is obtained by projecting the unit normal vector $\vec{n}(s)$ on the respective frame at the location s. To determine the circumferential position of the i-th point relative to the inner curvature reference point, a vector $\vec{v}(s,i)$ is defined from the centroid $\vec{c}(s)$ to the i-th point of the lumen contour $\vec{f}(s,i)$ of the IVUS frame at location s. Finally, $\kappa_{\text{idx}}(s,i)$ can be obtained using the dot product:

$$\vec{v}(s,i) = \vec{f}(s,i) - \vec{c}(s) \tag{8}$$

$$\kappa_{\text{idx}}(s,i) = \kappa(s)\,\vec{n}(s) \cdot \left(\frac{\vec{v}(s,i)}{\|\vec{v}(s,i)\|} \right) \tag{9}$$

As an example, Figure 7(c) shows a color-coded plaque-thickness distribution in a geometrically correct 3-D representation, with red indicating high and blue indicating low plaque thickness, normalized over the entire vessel segment. As described above, a curvature index was determined for each circumferential location on the contour. Figure 7(d) shows the color-coded curvature-index distribution, with red indicating inner curvature and blue indicating outer curvature.

2.5.2 Coronary Hemodynamics

The blood flow through the coronary arteries is simulated and the wall shear stress distribution determined using *computational fluid dynamics* (CFD) methodology. Tetrahedral meshing of the lumen using commercially available meshing software (Gambit, Fluent Inc., Lebanon NH, U.S.A.) provides an unstructured grid for simulations with U^{2}RANS, a well-validated CFD solver developed at The University of Iowa (Lai and Przekwas, 1994; Ramaswamy et al., 2004). An example for a tetrahedral mesh used as input for the CFD analysis is shown in Figure 8. Employing the computational mesh created in the reconstructed geometry of the arterial segment, and the specification of the appropriate boundary conditions, the governing equations of motion for the fluid are solved by U^{2}RANS to compute the velocity and pressure fields in the region of interest. For more details, see Lai and Przekwas (1994). Steady flow in the end-diastolic phase has been chosen for this study, although we can also perform moving-grid simulations with unsteady flow, at the cost of increased computational expense (Ramaswamy et al., 2004).

Blood is treated as an incompressible, homogenous, and Newtonian fluid. To allow the flow to be fully developed at the inlet, the 3-D model of the vessel is extended by 10× the inlet diameter at the ostium and 5× the outlet diameter at the distal end. Further, the no-slip boundary condition is specified at the vessel wall and a constant pressure outlet condition is utilized in the CFD model. The mean flow rate through the left main coronary artery has been reported to be around 100–120 ml/min (Sabbah et al., 1984; Perktold et al., 1998). Since the flow rate could not be measured in each of the coronary arteries during data acquisition for each patient due to procedural limitations, we consequently assumed a flow rate of 100 ml/min for all the coronary arterial segments employed in this analysis.

Positive and negative wall shear stress values are determined at each circumferential lumen location and mapped onto the 72 lumen vertices for each contour of the perpendicularly reoriented 3-D model. While the scalar wall-shear stress value (τ) can be determined directly at the lumen/plaque border, the directional component has to be determined in a small distance from the border due to the zero-velocity vectors at the border itself. The axial wall shear stress (τ_w), the component of interest in these simulations, is computed employing the relationship

$$\tau_w = \mu \left(\frac{dw}{dr} \right)_{r=a} \tag{10}$$

In this equation, μ is the viscosity coefficient, w is the axial velocity component, r is the radial coordinate, and a is the radius of the arterial segment. The velocity gradient (dw/dr) is computed at the wall to determine the axial wall shear stress. After the simulation, the directional τ-values are associated with the contour points. Any other data from inside the vessel or from the extensions are excluded from subsequent analysis.

2.6 Classification of Circumferential Regions

Each of the 72 circumferential locations in each vessel cross section is categorized with respect to its relative plaque thickness (above or below average for this cross section), its location relative to the local vessel curvature (inner or outer curvature), and its wall shear stress (above or below cross-sectional average). In this way, eight different "regions" result. The data has to be smoothed with a moving 45°-wedge over 5 frames to limit the impact of local noise. Also, a ninth "neutral" region includes those areas of curvature magnitude below a certain threshold, which are eliminated from analysis to avoid distortion of the results by low-curvature regions.

The following two quantitative indices separately correlate plaque distribution with curvature and plaque distribution with wall shear stress. The corresponding studies are described in Section 3.

2.6.1 Index for Correlation of Plaque Distribution and Curvature

To verify the observation that plaque tends to accumulate at the inner bend of the curvature rather than at the outer bend of the curvature, the relative portion r_{PC} of regions where inner curvature coincides with above-average plaque accumulation, or outer curvature coincides with below-average plaque accumulation, is determined. The ratio r_{PC} represents a "plaque/curvature index" with a value r_{PC}>0.5 indicating that more plaque has accumulated circumferentially along the inner curvature as compared to the outer curvature, thus supporting the hypothesis. Four regions are defined, as depicted in Figure 7(e): R_{ai} (red), R_{ao} (magenta), R_{bi} (yellow), and R_{bo} (blue); the "neutral" region R_n of local below-threshold curvature is colored in green. These regions represent pairs distinguishing circumferentially "above-average" plaque thickness (a) from "below-average" plaque thickness (b), coinciding with either "inner curvature" (i) or "outer curvature" (o) of the vessel wall. Thus, the plaque/curvature index is defined as

$$r_{PC} = \frac{\|R_{ai} + R_{bo}\|}{\|R_{ai} + R_{bo} + R_{ao} + R_{bi}\|} \tag{11}$$

2.6.2 Index for Correlation of Plaque Distribution and Wall Shear Stress

In analogy to the r_{PC} index, the relative portion r_{PW} of elements for which circumferentially above-average plaque thickness coincides with below-average wall shear stress (and vice versa) is determined for each vessel segment. By replacing "inner curvature" (i) with "lower-than-average wall shear stress" (l) and "outer curvature" (o) with "higher-than-average wall shear stress" (h) in Eq. (11),

$$r_{PW} = \frac{\|R_{al} + R_{bh}\|}{\|R_{al} + R_{bh} + R_{ah} + R_{bl}\|} \tag{12}$$

yields the definition for the plaque/wall-shear-stress index.

3 Studies and Results

Except for the new developments in IVUS segmentation presented in this paper, the validation of our methodology has been performed before and published previously. The fusion system was validated in computer simulations, phantoms, and in-vitro pig hearts as described in Wahle et al. (1999). The volumetric analysis was validated in computer phantoms (Medina et al., 2003), so were the curvature measurements and the curvature index (Medina et al., 2004). Therefore, the following subsections concentrate on IVUS validation as well as on the studies for analyzing the interdependencies between the circumferential plaque distribution and the curvature (Section 3.3) and between the circumferential plaque distribution and the local wall shear stress (Section 3.4). Additional study-specific methodologies are introduced as needed, and results are presented at the end of each subsection.

3.1 Acquitition of In-Vivo Patient Data

All procedures for acquisition of patient data were approved by the Human Subject Offices of the respective institutions. IVUS data were acquired using ClearView consoles with 40 MHz catheters with single rotating transducers (Boston Scientific Inc., Mountain View CA, U.S.A.), stored on S-VHS tape, and later digitized at 10–15 frames per second. Angiographic data showing the IVUS catheter and lumen outline was acquired using biplane and single-plane Philips Integris systems as well as single-plane Toshiba and General Electric systems, depending on the acquisition site. The angiograms were stored in DICOM format on CD-R and then directly imported into the fusion system as described in Olszewski et al. (2003).

3.2 Validation of the IVUS segmentation

The segmentation system was tested on a set of 21 in-vivo IVUS pullbacks containing a mixture of each of the three major coronary arteries [8 left anterior descending arteries (LAD), 8 right coronary arteries (RCA), 5 left circumflex arteries (LCX); 3288 total frames]. Following the optimal 3-D segmentation, lumen/plaque and media/adventitia borders were available for each vessel. These borders were compared with independent, expert-identified borders that had been manually traced as the gold standard (Olszewski et al., 2005). In each instance, the vessel being segmented was left out of the training set used for the cost function design. The differences between the detected borders and the manually traced borders were computed for 720 corre-

sponding points (every half degree angularly) on each border and are given in Table 1, showing no bias in segmentation and a maximum positional error of 0.236 mm for the lumen/plaque and 0.300 mm for the media/adventitia borders.

3.3 Correlating Plaque Distribution and Curvature

The index r_{PC} indicating the relative portion of regions where circumferentially the inner curvature coincided with above-average plaque accumulation, or the outer curvature coincided with below-average plaque accumulation, was determined in a set of 60 vessels [preliminary results in 37 vessels were reported in Wahle et al. (2004)].

3.3.1 Impact of Curvature Threshold and Vessel Type

Twelve different threshold values were empirically selected ranging from 2.31 to 22.94°/cm, resulting in 10.1–77.8% of circumferential locations being assigned to the neutral region R_n, as colored green in the example in Figure 7(e). The thresholds were chosen to exclude from 5° (lowest threshold) to 60° (highest threshold) of each 90° quadrant of an IVUS frame in the analysis, based on the average maximum curvature of the vessels in this study. The results are depicted in Figure 9. The chart shows that the average r_{PC} over all 60 vessels increases steadily with the increase of the curvature threshold. Thus, the more regions of low curvature that were included into R_n and, therefore, increased the proportion of higher curvature regions that were included in the calculation of r_{PC}, the more the hypothesis was supported.

The increase in standard deviation of r_{PC} prompted us to categorize the results by vessel (Tab. 2). For this purpose, the number of thresholds was determined (out of the 12 selected ones shown in Fig. 9) for which $r_{PC}>0.5$ was satisfied. While almost two thirds of the vessels satisfied $r_{PC}>0.5$ for *all* thresholds, the hypothesis was more strongly supported in LAD arteries (87% for all, or at least half, of the thresholds). The results in the RCA and LCX arteries were less supportive.

3.3.2 Impact of Interventions

Stenting may have a substantial impact on the outcome of the plaque/curvature index r_{PC}. Preliminary results of a study reported in Lopez et al. (2005) showed that soft plaque is mainly circumferentially redistributed within the stented area, whereas hard plaque was mainly compressed. In several of the vessels analyzed, a below-threshold value of r_{PC} ($r_{PC}<0.5$) was determined when all segments were included and only branch locations were excluded. After also excluding known regions of intervention and stenting, $r_{PC}>0.5$ was reached, frequently showing the increase of r_{PC} with the increase in curvature threshold (Figs. 10, 11). This contradicts our initially reported findings in a smaller subset of patients (Wahle et al., 2004) in which

the plaque/curvature index r_{PC} was not significantly different whether or not stented regions were included in the analysis. Our new results rather suggest that substantial disease and stenting *may* have an effect on the relation between vessel geometry and plaque distribution.

3.4 Correlating Plaque Distribution and Wall Shear Stress

We analyzed 48 vessels (a subset of Section 3.3, since some parameters were not available for vessels received from collaborating sites) for an inverse correlation of circumferential plaque distribution and corresponding local wall shear stress. The study had to be performed in four increasingly restrictive subsets of data, since a direct correlation could not be found. This becomes obvious when revisiting the process of remodeling.

While disease progression and stenting impact the curvature/plaque relationship to some extent, an even more substantial effect can be expected for the wall shear stress distribution. The distribution is substantially altered when the limits of positive remodeling are reached (Wentzel et al., 2003b). Thus, the vessel subsegments for which the area stenosis is between 10% and 40% are of particular interest [the compensatory-enlargement range identified by Glagov et al. (1987)]. Consequently, we concentrated on whether and how significantly the correlation improves once vessel segments of certain properties are excluded from the analysis. In this way, indirect evidence of which local conditions favor the underlying hypothesis of below-average wall shear stress inducing above-average plaque thickness was sought.

3.4.1 Grouping of Vessels and Segments by Disease Severity

First, the relative portion r_{PW} of elements for which circumferentially above-average plaque thickness coincides with below-average wall shear stress (and vice versa) was determined for each vessel segment as explained in Section 2.6.2. This step created Set #1. Next, all vessel subsegments that included vessel branching areas, stents, or regions of dense calcification were excluded, forming Set #2. Within Set #2, percent-area stenosis was determined for each frame following Glagov's definition, which does not require the presence of a normal reference segment (plaque+wall area over cross-sectional vessel area) (Glagov et al., 1987). Set #3 consisted of all such vessels from Set #2 for which the percent-area stenosis was in the range of 10–40% in at least 35% of the non-excluded vessel segments. Set #3 consisted of 31 vessels satisfying this criterion. In each vessel, the segments of Sets #2 and #3 that were within the 10–40% range of area stenosis formed Subsets #2a and #3a. The 35% cut-off value was determined empirically as the minimum percent value of the largest cluster for which the r_{PW} values in Set #2a improved over Set #2.

An illustration for the definition of these sets is shown in Figure 12: Vessel 1 shows

only minor disease, whereas Vessel 2 is subject to advanced atherosclerosis; both form Set #1. For Vessel 1, all subsegments are retained when proceeding to Set #2, whereas two subsegments of Vessel 2 were discarded due to calcifications. All subsegments outside the 10–40% area stenosis range are removed from Set #2 to create Set #2a, thus discarding one subsegment from Vessel 1 and two subsegments from Vessel 2. Only Vessel 1 proceeds from Set #2 to Set #3, since less than 35% of Vessel 2 are within the 10–40% area stenosis range. For Vessel 1, in analogy to the step from Set #2 to Set #2a, the center segment is discarded from Set #3 to Set #3a.

3.4.2 Hypothesis Test

If the hypothesis is correct and observable in regions where severe luminal narrowing is not present, the vessels in Subsets #2a and #3a should provide higher r_{PW} ratios than the corresponding vessels in Sets #2 and #3. Therefore, we determined factors g_{PW} quantifying the change $g_{PW\{2\}} = r_{PW\{2a\}}/r_{PW\{2\}}$ for all vessels and $g_{PW\{3\}} = r_{PW\{3a\}}/r_{PW\{3\}}$ for vessels with the minimum of 35% of frames within the 10–40% area-stenosis range. Note that the $g_{PW\{x\}}$ represent the differences in hypothesis validity. Consequently, $g_{PW\{x\}}>1$ suggests a case for which the hypothesis is more strongly supported in those segments of vessel x with compensatory enlargement as compared to those with lumen narrowing. The analysis rationale is to determine: (1) whether applying the hypothesis test on the subset of segments defined in Set #2a (10–40% stenosis) increases the validity of the hypothesis compared to the Set #2; and, (2) whether applying the hypothesis test on Set #3a (10–40% stenosis in vessels with ≥35% of the wall within this range) increases the hypothesis validity compared to the Set #3 (≥35% of the wall within the 10–40% stenosis range).

3.4.3 Changes in Hypothesis Validity

The results are summarized in Table 3 ($g_{PW\{x\}}\geq1.01$ is considered an "increase" and $g_{PW\{x\}}\leq0.99$ a "decrease"). The significance of the increase of the r_{PW} ratios between Sets #2a/#2 and Sets #3a/#3, respectively, was determined by a paired t-test for means with null-hypothesis. As can be seen from Table 3, 19 out of 31 (or 61%) vessels in Sets #3a/#3 were in the $g_{PW\{x\}}\geq1.01$ category, whereas only 25 out of 48 (52%) in Sets #2a/#2 were in the $g_{PW\{x\}}\geq1.01$ category. The majority of the vessels contained in Set #2 but not in Set #3 were in the $g_{PW\{x\}}\leq0.99$ category. Thus, hypothesis validity improves and becomes statistically significant in Sets #3a/#3 vs. Sets #2a/#2, confirming our assumption. A notable cluster of 12 vessels in Set #3, having 35–63% of frames in the 10–40% area-stenosis range, showed an average 10.2% increase in hypothesis validity which was highly significant ($p<0.001$). This can be explained, in part, by the minimization of statistical noise with an even distribution of frames within vs. outside of the 10–40% area-stenosis range.

4 Discussion

The presented studies analyzed the relationships between circumferential plaque distribution and local vessel curvature as well as between circumferential plaque distribution and wall shear stress. Common hypotheses that plaque tends to accumulate more frequently on the inner curvature and thus at locations of relatively low wall shear stress were verified on human in-vivo patient data. To obtain 3-D representations of the vessel segments in highest accuracy, our well-established and validated fusion methodology was employed. Novel IVUS segmentation methodology was developed to more efficiently utilize the 3-D context of the data, previously expert-traced IVUS contours, and the physical properties of ultrasound. In total, IVUS and angiographic data from 48 vessels (60 for the plaque/curvature study) were available to obtain a sufficient statistical base for the analyses.

A system for the automated segmentation of IVUS images has been presented. The design of the cost function, coupled with a 3-D globally optimal graph-based segmentation routing gives the system a distinct advantage over current systems. The design incorporates both learned and analytic terms in multiple scales to obtain a robust segmentation. As an added benefit of using a learning algorithm, the new system also has the ability to continue learning over time and, hence, the ability to get better with age. Results show that the system agrees with expertly traced contours in a number of clinical datasets.

The study correlating plaque distribution and curvature showed that indeed plaque accumulates more frequently on the inner curvature than at the outer curvature in the majority of vessels. The LAD artery showed the best results, which can be explained by its relatively fair correspondence to a curved-tube model (Agrawal, 1975; Agrawal et al., 1978). The RCA and LCX vessels have a more complex (and more tortuous) shape than the LAD and provide less support for the hypothesis. This was likely caused by the more complex flow patterns in these vessels that can no longer be explained by the curved-tube model. Another factor was the impact of interventions, which frequently distort an otherwise good correlation between plaque distribution and local curvature. As part of this study, we analyzed the impact of PTCA and stenting on the correlation between plaque distribution and curvature. Depending on the plaque composition, plaque is either compressed (in calcific "hard" plaques), or circumferentially redistributed while retaining its volume (Lopez et al., 2005). Also, stenting may distort the overall vessel geometry by a stretching effect as reported by von Birgelen et al. (2003). Consequently, we excluded stented segments from the following steps of the analysis.

While the curvature in general is only moderately influenced by plaque progression, flow patterns and consequently the wall shear stress distribution substantially change once luminal narrowing occurs (Wentzel et al., 2003b). It was therefore feasible to assume that a correlation between circumferential plaque distribution and relatively low

wall shear stress primarily applies to those vessel segments which show compensatory enlargement but no luminal narrowing. Based on the work of Glagov et al. (1987), the threshold was set at 40% area stenosis. An IVUS-fusion study performed in 55 vessels (all <50% area stenosis) of 40 patients showed positive remodeling in 81% of the cases (Feldman et al., 2006), thus confirming the validity of this assumption. While confirming the observations described by Wentzel et al. (2003b), our study introduces an essentially automated sorting process based on the atherosclerotic stage of each individual vessel segment. This process reduces time and effort necessary to perform such an analysis after the 3-D vascular models are generated.

The correlation of plaque distribution with curvature is much stronger than with wall shear stress. While we were unable to show a *direct* correlation of low wall shear stress and increased plaque accumulation, there was *indirect* evidence that such correlations apply to vessel subsegments with compensatory enlargement but without luminal narrowing, as expected. However, this indirect evidence is only statistically significant as long as a sufficient portion of vessel subsegments are undergoing compensatory enlargement. If less than 35% of vessel subsegments remain in the compensatory-enlargement phase, no significant correlation can be seen. It has to be kept in mind that this cut-off value was determined empirically and may have to be adjusted after including more patient data, but we assume that this value is sufficiently representative. This would indicate that the flow patterns responsible for the wall shear stress distribution are highly affected by the subsegments in later disease stages, thus impacting and eliminating the overall correlation.

The presented studies are subject to a couple of limitations. Due to the additional effort necessary to accurately reflect vessel movement over the cardiac cycle, we used only end-diastolic 3-D data and steady-flow simulations. Since the time-averaged axial wall shear stress between simulations of steady flow and unsteady flow without arterial motion were shown to be comparable (Ramaswamy et al., 2004), the steady-flow simulation is likely less of an issue than the lack of a 4-D moving grid. Improvements in both the segmentation methodology and the efficiency of moving-grid unsteady-flow CFD simulations, along with faster hardware, should allow 4-D analyses in larger sets of data in the future.

Since most patients in this study suffered from advanced coronary artery disease, the relationships we observed were between a substantially altered coronary morphology and the related (altered) hemodynamic shear stress conditions. Instead of just grouping vessels into subsegments of advanced or lesser disease at a single snapshot in time, it would certainly be desirable to have multiple (longitudinal) 3-D or 4-D models for the same vessel available. This would allow a more accurate comparison of the predicted plaque progression, based on the initial plaque distribution and wall shear stresses, with the actual plaque distribution as developed after a certain time has passed. Unfortunately, follow-up in-vivo data are rarely available in a sufficiently large number of patients. Nevertheless, the indirect evidence gathered from a single snapshot in time is sufficiently conclusive and statistically significant.

5 Conclusions

Plaque development depends on the wall shear stress distribution, which in turn depends on the vessel geometry. The presented in-vivo studies demonstrate that circumferential plaque distribution correlates with local vessel curvature, and also correlates with wall shear stress in early stages of atherosclerosis. To facilitate our study, a novel IVUS segmentation based on optimum 3-D graph search was employed, in order to minimize time and manual effort for segmenting the IVUS data. Our results suggest that the correlation is much more pronounced between circumferential plaque distribution and local curvature than between plaque distribution and wall shear stress, which may qualify curvature as a more easily applied clinical marker for practical reasons. Our studies show that, in the majority of vessels, plaque tends to form at the inner curvature of the vessel wall. These findings suggest that low wall shear stress, which is typically associated with inner vessel curvature locations, likely contributes to the *initial* formation of atherosclerotic plaque in human coronary arteries. We have demonstrated that the hypothesis of above-average plaque thickness being associated with below-average wall shear stress is more strongly supported in *early* stages of disease progression than it is in *later* stages of atherosclerosis when positive remodeling can no longer compensate for the disease and the lumen narrows.

Acknowledgments

This work has been supported in part by grant R01 HL063373 of the National Heart, Lung, and Blood Institute at the National Institutes of Health, Bethesda MD, U.S.A. The authors would like to thank Theresa M. H. Brennan and Kathleen C. Braddy from the University of Iowa, as well as Elizabeth M. Holper, Syed W. Bokhari, and J. Gray Bennett from the University of Chicago, for their efforts in the acquisition of in-vivo patient data; Xiaodong Wu and Kang Li, University of Iowa, for their methodology and support for optimal surface detection; Rubén Medina, Universidad de Los Andes, Facultad de Ingeniería, Mérida (Venezuela), for his contributions to the curvature-index determination; as well as Peter H. Stone and Charles L. Feldman, both Brigham & Women's Hospital, Cardiovascular Division, Boston MA, and A. Ümit Coşkun, Northeastern University, Mechanical / Industrial / Manufacturing Engineering, Boston MA, for their contributions, the additional in-vivo patient data for the plaque/curvature study, and fruitful discussions on wall shear stresses.

References

Agrawal, Y. C., 1975. Laser velocimeter study of entrance flows in curved pipes. Ph.D. Thesis, University of California at Berkeley, United States.

Agrawal, Y. C., Talbot, L., Gong, K., 1978. Laser anemometer study of flow development in curved circular pipes. Journal of Fluid Mechanics 85 (3), 497–518.

Bao, Y., Oswald, H., Fleck, E., 1990. The pyramid structure and its application to binary image reconstruction from two projections. In: Proc. International Conference on Acoustics, Speech, and Signal Processing (ICASSP-90). Vol. 4. IEEE Press, Piscataway NJ, pp. 1845–1848.

Beier, J., Oswald, H., Sauer, H. U., Fleck, E., 1991. Accuracy of measurement in quantitative coronary angiography (QCA). In: Lemke, H. U., Rhodes, M. L., Jaffe, C. C., Felix, R. (Eds.), Computer Assisted Radiology (CAR '91). Springer, Berlin/New York, pp. 721–726.

Brown, B. G., Bolson, E. L., Frimer, M., Dodge, H. T., Feb. 1977. Quantitative coronary arteriography; estimation of dimensions, hemodynamic resistance, and atheroma mass of coronary artery lesions using the arteriogram and digital computation. Circulation 55 (2), 329–337.

Brown, B. G., Simpson, P., Dodge, J. T., Bolson, E. L., Dodge, H. T., 1991. Quantitative and qualitative coronary arteriography. In: Reiber, J. H. C., Serruys, P. W. (Eds.), Quantitative Coronary Arteriography. Vol. 117 of Developments in Cardiovascular Medicine. Kluwer, Dordrecht, pp. 3–21.

Brusseau, E., de Korte, C. L., Mastik, F., Schaar, J., van der Steen, A. F. W., May 2004. Fully automatic luminal contour segmentation in intracoronary ultrasound imaging — a statistical approach. IEEE Transactions on Medical Imaging 23 (5), 554–566.

Burckhardt, C. B., January 1978. Speckle in ultrasound B-mode scans. IEEE Transactions on Sonics and Ultrasonics SU-25 (1), 1–6.

Chakraborty, A., Staib, L. H., Duncan, J. S., December 1996. Deformable boundary finding in medical images by integrating gradient and region information. IEEE Transactions on Medical Imaging 15 (6), 859–870.

Chan, T. F., Vese, L. A., February 2001. Active contours without edges. IEEE Transactions on Image Processing 10 (2), 266–277.

Evans, J. L., Ng, K. H., Wiet, S. G., Vonesh, M. J., Burns, W. B., Radvany, M. G., Kane, B. J., Davidson, C. J., Roth, S. I., Kramer, B. L., Meyers, S. N., McPherson, D. D., Feb. 1996. Accurate three-dimensional reconstruction of intravascular ultrasound data; spatially correct three-dimensional reconstructions. Circulation 93 (3), 567–576.

Feldman, C. L., Coşkun, A. Ü., Yeghiazarians, Y., Kinlay, S., Wahle, A., Olszewski, M. E., Rossen, J. D., Sonka, M., Popma, J. J., Orav, J., Kuntz, R. E., Stone, P. H., Jan. 2006. Remodeling characteristics of minimally diseased coronary arteries are consistent along the length of the artery. American Journal of Cardiology 97 (1), 13–16.

Friedman, M. H., Bargeron, C. B., Deters, O. J., Hutchins, G. M., Mark, F. F., Nov. 1987. Correlation between wall shear and intimal thickness at a coronary artery

branch. Atherosclerosis 68 (1/2), 27–33.

Gibson, C. M., Diaz, L., Kandarpa, K., Sacks, F. M., Pasternak, R. C., Sandor, T., Feldman, C. L., Stone, P. H., Feb. 1993. Relation of vessel wall shear stress to atherosclerosis progression in human coronary arteries. Arteriosclerosis and Thrombosis 13 (2), 310–315.

Glagov, S., Weisenberg, E., Zarins, C. K., Stankunavicius, R., Kolettis, G. J., May 1987. Compensatory enlargement of human atherosclerotic coronary arteries. New England Journal of Medicine 316 (22), 1371–1375.

Herrington, D. M., Johnson, T., Santago, P., Snyder, W. E., 1992. Semi-automated boundary detection for intravascular ultrasound. In: Proc. Computers in Cardiology 1992, Durham NC. IEEE-CS Press, Los Alamitos CA, pp. 103–106.

Kass, M., Witkin, A., Terzopulous, D., 1988. Snakes: Active contour models. International Journal of Computer Vision 1 (4), 321–331.

Kirkeeide, R. L., Fung, P., Smalling, R. W., Gould, K. L., 1982. Automated evaluation of vessel diameter from arteriograms. In: Proc. Computers in Cardiology 1982, Seattle WA. IEEE-CS Press, Los Alamitos CA, pp. 215–218.

Klingensmith, J. D., Schoenhagen, P., Tajaddini, A., Halliburton, S. S., Tuzcu, E. M., Nissen, S. E., Vince, D. G., May 2003. Automated three-dimensional assessment of coronary artery anatomy with intravascular ultrasound scanning. American Heart Journal 145 (5), 795–805.

Klingensmith, J. D., Shekhar, R., Vince, D. G., Oct. 2000. Evaluation of three-dimensional segmentation algorithms for the identification of luminal and medial-adventitial borders in intravascular ultrasound images. IEEE Transactions on Medical Imaging 19 (10), 996–1011.

Laban, M., Oomen, J. A., Slager, C. J., Wentzel, J. J., Krams, R., Schuurbiers, J. C. H., den Boer, A., von Birgelen, C., Serruys, P. W., de Feyter, P. J., 1995. ANGUS: A new approach to three-dimensional reconstruction of coronary vessels by combined use of angiography and intravascular ultrasound. In: Proc. Computers in Cardiology 1995, Vienna AT. IEEE Press, Piscataway NJ, pp. 325–328.

Lai, Y. G., Przekwas, A. J., 1994. A finite-volume method for fluid flow simulations with moving boundaries. Computational Fluid Dynamics 2, 19–40.

Li, K., Chen, D., Sonka, M., 2004a. Efficient optimal surface detection: Theory, implementation and experimental validation. In: Sonka, M., Fitzpatrick, J. M. (Eds.), Medical Imaging 2004: Image Processing. Vol. 5370. SPIE Proceedings, Bellingham WA, pp. 620–627.

Li, K., Wu, X., Chen, D. Z., Sonka, M., June 2004b. Globally optimal segmentation of interacting surfaces with geometric constraints. In: Proceedings, IEEE Computer Society Conference on Computer Vision and Pattern Recognition (CVPR). IEEE Press, Piscataway, NJ, pp. 394–399.

Li, W., von Birgelen, C., Di Mario, C., Boersma, E., Gussenhoven, E. J., van der Putten, N. H. J. J., Bom, N., 1994/95. Semi-automatic contour detection for volumetric quantification of intravascular ultrasound. In: Proc. Computers in Cardiology 1994, Bethesda MD. IEEE-CS Press, Los Alamitos CA, pp. 277–280.

Liang, Q., Wendelhag, I., Wikstrand, J., Gustavsson, T., February 2000. A multiscale dynamic programming procedure for boundary detection in ultrasonic artery

images. IEEE Transactions on Medical Imaging 19 (2), 127–142.

Lopez, J. J., Wahle, A., Olszewski, M. E., Gualano, S., Bokhari, S. W., Bennett, J. G., Vigmostad, S. C., Medina, R., Sonka, M., May 2005. Differential effects of coronary stenting on calcified and non-calcified vessels: Reanalysis of the mechanism of lumen enlargement by quantitative analysis of plaque redistribution with 3-D IVUS/angiography fusion. Society for Cardiovascular Angiography and Interventions, 28th Annual Scientific Sessions, Ponte Vedra FL, Catheterization and Cardiovascular Interventions (Supplement) 65 (1), 131, abstract C-23.

Medina, R., Wahle, A., Olszewski, M. E., Sonka, M., Aug. 2003. Three methods for accurate quantification of plaque volume in coronary arteries. International Journal of Cardiovascular Imaging 19 (4), 301–311.

Medina, R., Wahle, A., Olszewski, M. E., Sonka, M., 2004. Curvature and torsion estimation for coronary artery motion analysis. In: Amini, A. A., Manduca, A. (Eds.), Medical Imaging 2004: Physiology, Function, and Structure from Medical Images. Vol. 5369. SPIE Proceedings, Bellingham WA, pp. 504–515.

Mojsilović, A., Popović, M., Amodaj, M., Babić, R., Ostojić, M., Nov./Dec. 1997. Automatic segmentation of intravascular ultrasound images; A texture-based approach. Annals of Biomedical Engineering 25 (6), 1059–1071.

Nair, A., Kuban, B. D., Tuzcu, E. M., Schoenhagen, P., Nissen, S. E., Vince, D. G., Oct. 2002. Coronary plaque classification with intravascular ultrasound radiofrequency analysis. Circulation 106 (17), 2200–2206.

Olszewski, M. E., Wahle, A., Medina, R., Mitchell, S. C., Sonka, M., 2003. Integrated system for quantitative analysis of coronary plaque via data fusion of biplane angiography and intravascular ultrasound. In: Lemke, H. U., Inamura, K., Vannier, M. W., Farman, A. G., Doi, K., Reiber, J. H. C. (Eds.), Computer Assisted Radiology and Surgery (CARS 2003). Vol. 1256 of Excerpta Medica International Congress Series. Elsevier, Amsterdam, pp. 1117–1122.

Olszewski, M. E., Wahle, A., Vigmostad, S. C., Sonka, M., 2005. Multidimensional segmentation of coronary intravascular ultrasound images using knowledge-based methods. In: Fitzpatrick, J. M., Reinhardt, J. M. (Eds.), Medical Imaging 2005: Image Processing. Vol. 5747. SPIE Proceedings, Bellingham WA, pp. 496–504.

Pellot, C., Bloch, I., Herment, A., Sureda, F., May/Jun. 1996. An attempt to 3-D reconstruct vessel morphology from X-ray projections and intravascular ultrasounds modeling and fusion. Computerized Medical Imaging and Graphics 20 (3), 141–151.

Pellot, C., Herment, A., Sigelle, M., Horain, P., Maître, H., Peronneau, P., Mar. 1994. A 3D reconstruction of vascular structures from two X-ray angiograms using an adapted simulated annealing algorithm. IEEE Transactions on Medical Imaging 13 (1), 48–60.

Perktold, K., Hofer, M., Rappitsch, G., Loew, M., Kuban, B. D., Friedman, M. H., Mar. 1998. Validated computation of physiologic flow in a realistic coronary artery branch. Journal of Biomechanics 31 (3), 217–228.

Prause, G. P. M., DeJong, S. C., McKay, C. R., Sonka, M., 1996. Semi-automated segmentation and 3-D reconstruction of coronary trees: Biplane angiography and intravascular ultrasound data fusion. In: Hoffman, E. A. (Ed.), Medical Imaging 1996: Physiology and Function from Multidimensional Images. Vol. 2709. SPIE

Proceedings, Bellingham WA, pp. 82–92.

Prause, G. P. M., Onnasch, D. G. W., Aug. 1996. Binary reconstruction of the heart chambers from biplane angiographic image sequences. IEEE Transactions on Medical Imaging 15 (4), 532–546.

Ramaswamy, S. D., Vigmostad, S. C., Wahle, A., Lai, Y. G., Olszewski, M. E., Braddy, K. C., Brennan, T. M. H., Rossen, J. D., Sonka, M., Chandran, K. B., Dec. 2004. Fluid dynamic analysis in a human left anterior descending coronary artery with arterial motion. Annals of Biomedical Engineering 32 (12), 1628–1641.

Reiber, J. H. C., Gerbrands, J. J., Troost, G. J., Kooijman, C. J., Slump, C. H., 1982/83. 3-D reconstruction of coronary arterial segments from two projections. In: Heintzen, P. H., Brennecke, R. (Eds.), Digital Imaging in Cardiovascular Radiology. Thieme, Stuttgart/New York, pp. 151–163.

Reiber, J. H. C., Koning, G., Dijkstra, J., Wahle, A., Goedhart, B., Sheehan, F. H., Sonka, M., 2000. Angiography and intravascular ultrasound. In: Sonka, M., Fitzpatrick, J. M. (Eds.), Handbook of Medical Imaging — Volume 2: Medical Image Processing and Analysis. SPIE Press, Bellingham WA, pp. 711–808.

Sabbah, H. N., Walburn, F. J., Stein, P. D., Aug. 1984. Patterns of flow in the left coronary artery. Journal of Biomechanical Engineering 106 (3), 272–279.

Seiler, C., Kirkeeide, R. L., Gould, K. L., Jun. 1992. Basic structure-function relations of the epicardial coronary vascular tree; basis of quantitative coronary arteriography for diffuse coronary artery disease. Circulation 85 (6), 1987–2003.

Shekhar, R., Cothren, R. M., Vince, D. G., Cornhill, J. F., 1996. Fusion of intravascular ultrasound and biplane angiography for three-dimensional reconstruction of coronary arteries. In: Proc. Computers in Cardiology 1996, Indianapolis IN. IEEE Press, Piscataway NJ, pp. 5–8.

Sonka, M., Winniford, M. D., Collins, S. M., Mar. 1995a. Robust simultaneous detection of coronary borders in complex images. IEEE Transactions on Medical Imaging 14 (1), 151–161.

Sonka, M., Zhang, X., Siebes, M., Bissing, M. S., DeJong, S. C., Collins, S. M., McKay, C. R., Dec. 1995b. Segmentation of intravascular ultrasound images: A knowledge-based approach. IEEE Transactions on Medical Imaging 14 (4), 719–732.

Stary, H. C., Chandler, A. B., Dinsmore, R. E., Fuster, V., Glagov, S., Insull, W., Rosenfeld, M. E., Schwartz, C. J., Wagner, W. D., Wissler, R. W., Sep. 1995. A definition of advanced types of atherosclerotic lesions and a histological classification of atherosclerosis: A report from the committee on vascular lesions of the council on arteriosclerosis, American Heart Association. Arteriosclerosis, Thrombosis, and Vascular Biology 15 (9), 1512–1531.

Stary, H. C., Chandler, A. B., Glagov, S., Guyton, J. R., Insull, W., Rosenfeld, M. E., Schaffer, S. A., Schwartz, C. J., Wagner, W. D., Wissler, R. W., May 1994. A definition of initial, fatty streak, and intermediate lesions of atherosclerosis: A report from the committee on vascular lesions of the council on arteriosclerosis, American Heart Association. Arteriosclerosis and Thrombosis 14 (5), 840–856.

Stone, P. H., Coşkun, A. Ü., Kinlay, S., Clark, M. E., Sonka, M., Wahle, A., Ilegbusi, O. J., Yeghiazarians, Y., Popma, J. J., Orav, J., Kuntz, R. E., Feldman, C. L., Jul. 2003. Effect of endothelial shear stress on the progression of coronary artery disease,

vascular remodeling, and in-stent restenosis in man; in-vivo 6-month followup study. Circulation 108 (4), 438–444.

van der Zwet, P. M. J., Reiber, J. H. C., Jul. 1994. A new approach for the quantification of complex lesion morphology: The gradient field transform; basic principles and validation results. Journal of the American College of Cardiology 24 (1), 216–224.

von Birgelen, C., de Vrey, E. A., Mintz, G. S., Nicosia, A., Bruining, N., Li, W., Slager, C. J., Roelandt, J. R. T. C., Serruys, P. W., de Feyter, P. J., Nov. 1997. ECG-gated three-dimensional intravascular ultrasound: Feasibility and reproducibility of the automated analysis of coronary lumen and atherosclerotic plaque dimensions in humans. Circulation 96 (9), 2944–2952.

von Birgelen, C., Mintz, G. S., Eggebrecht, H., Herrmann, J., Jasper, M., Brinkhoff, J., Neumann, T., Böse, D., Baumgart, D., Schmermund, A., Wieneke, H., Haude, M., Erbel, R., Jul. 2003. Preintervention arterial remodeling affects vessel stretch and plaque extrusion during coronary stent deployment as demonstrated by 3-D intravascular ultrasound. American Journal of Cardiology 92 (2), 130–135.

Wagner, R. F., Smith, S. W., Sandrik, J. M., Lopez, H., May 1983. Statistics of speckle in ultrasound B-scans. IEEE Transactions on Sonics and Ultrasonics 30 (3), 156–163.

Wahle, A., Mitchell, S. C., Ramaswamy, S. D., Chandran, K. B., Sonka, M., 2001. Four-dimensional coronary morphology and computational hemodynamics. In: Sonka, M., Hanson, K. M. (Eds.), Medical Imaging 2001: Image Processing. Vol. 4322. SPIE Proceedings, Bellingham WA, pp. 743–754.

Wahle, A., Olszewski, M. E., Vigmostad, S. C., Medina, R., Coşkun, A. Ü., Feldman, C. L., Stone, P. H., Braddy, K. C., Brennan, T. M. H., Rossen, J. D., Chandran, K. B., Sonka, M., 2004. Quantitative analysis of circumferential plaque distribution in human coronary arteries in relation to local vessel curvature. In: Proc. 2004 IEEE International Symposium on Biomedical Imaging. IEEE Press, Piscataway NJ, pp. 531–534.

Wahle, A., Prause, G. P. M., DeJong, S. C., Sonka, M., Aug. 1999. Geometrically correct 3-D reconstruction of intravascular ultrasound images by fusion with biplane angiography — methods and validation. IEEE Transactions on Medical Imaging 18 (8), 686–699.

Wahle, A., Sonka, M., 2005. Coronary plaque analysis by multimodality fusion. In: Suri, J. S., Yuan, C., Wilson, D. L., Laxminarayan, S. (Eds.), Plaque Imaging: Pixel to Molecular Level. Vol. 113 of Studies in Health, Technology and Informatics. IOS Press, Amsterdam, pp. 321–359.

Wahle, A., Wellnhofer, E., Mugaragu, I., Sauer, H. U., Oswald, H., Fleck, E., Jun. 1995. Assessment of diffuse coronary artery disease by quantitative analysis of coronary morphology based upon 3-D reconstruction from biplane angiograms. IEEE Transactions on Medical Imaging 14 (2), 230–241.

Wentzel, J. J., Gijsen, F. J. H., Stergiopulos, N., Serruys, P. W., Slager, C. J., Krams, R., May 2003a. Shear stress, vascular remodeling and neointimal formation. Journal of Biomechanics 36 (5), 681–688.

Wentzel, J. J., Janssen, E., Vos, J., Schuurbiers, J. C. H., Krams, R., Serruys, P. W.,

de Feyter, P. J., Slager, C. J., Jul. 2003b. Extension of increased atherosclerotic wall thickness into high shear stress regions is associated with loss of compensatory remodeling. Circulation 108 (1), 17–23.

Zhang, X., McKay, C. R., Sonka, M., Dec. 1998. Tissue characterization in intravascular ultrasound images. IEEE Transactions on Medical Imaging 17 (6), 889–899.

	Lumen	Adventitia
Signed Mean ± SD (mm)	0.042 ± 0.062	-0.007 ± 0.108
Unsigned Mean ± SD (mm)	0.180 ± 0.027	0.200 ± 0.069
Maximum (mm)	0.236	0.300

Table 1
Segmentation border positioning errors.

	Number of curvature thresholds for which $r_{PC}>0.5$ is satisfied				
Vessel	12	≥6	≥1	=0	
LAD	17	3	1	2	*23*
RCA	10	4	1	8	*23*
LCX	9	1	0	4	*14*
	36	*8*	*2*	*14*	*60*

Table 2
Results categorized by curvature threshold and vessel, with $r_{PC}>0.5$ was true for all (12), at least half (≥6), at least one (≥1), or none (=0) of the curvature thresholds.

	$g_{PW\{x\}}$	≥1.01	<1.01 >0.99	<1.01 ≤0.99	*	
Sets #2a/#2	*n=48*	25	3	16	4	$p>0.75$
#3a/#3	*31*	19	3	7	2	$p<0.025$

Table 3
Results for the improvement $g_{PW\{x\}}$ in correlation of circumferentially lower wall shear stress with circumferentially higher plaque accumulation following exclusion of vessel subsegments outside the positive remodeling range; $*$: either all or none of the frames were within the 10–40% area-stenosis range, therefore $g_{PW\{x\}}$ was considered undefined, and these vessels were excluded from the p-value calculations.

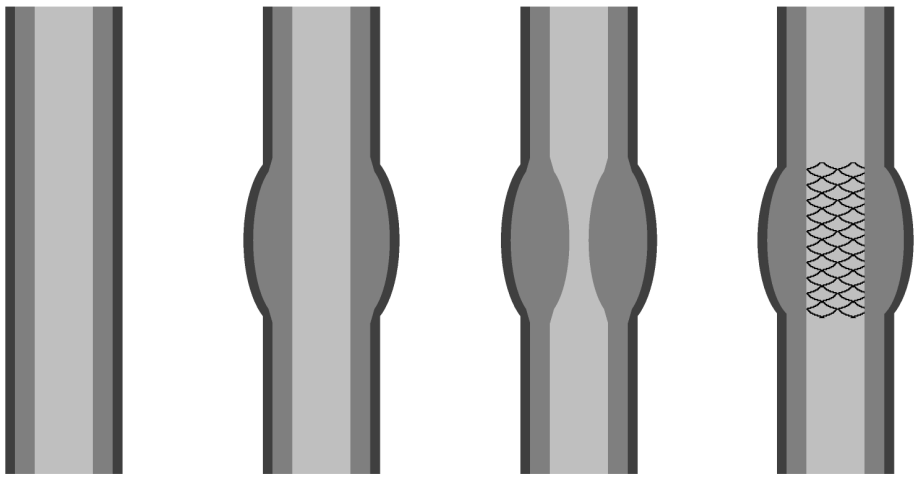

(a) (b) (c) (d)

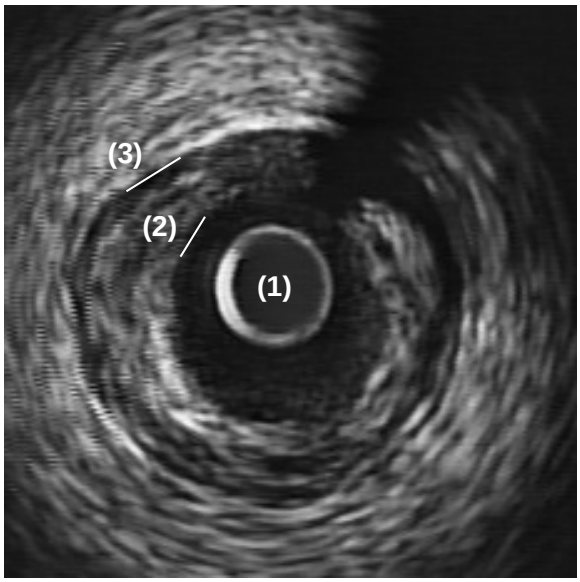

(e)

Fig. 1. Development of atherosclerotic plaque: lumen — light gray, plaque/intima — mid gray, media — dark gray; (a) vessel without any stenosis; (b) compensatory enlargement; (c) luminal narrowing; (d) after treatment with PTCA and stenting; (e) IVUS image with (1) catheter, (2) lumen/plaque, and (3) media/adventitia borders.

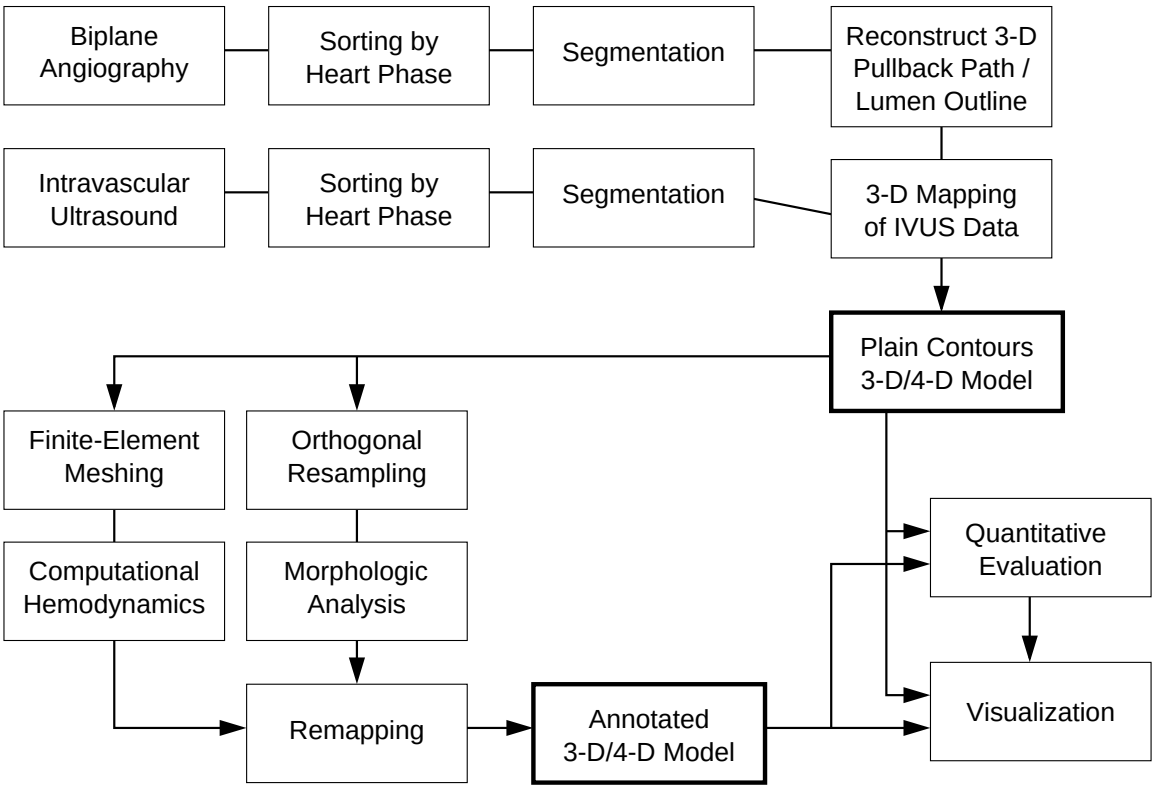

Fig. 2. Processing of the data from acquisition over segmentation to the generation of the *plain* model, followed by quantitative analyses used to *annotate* the 3-D/4-D model.

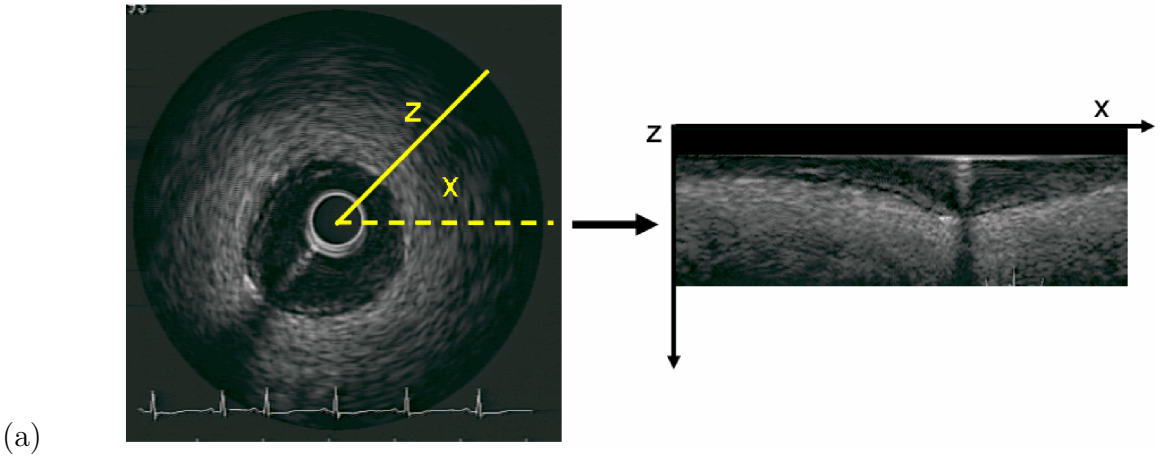

(a)

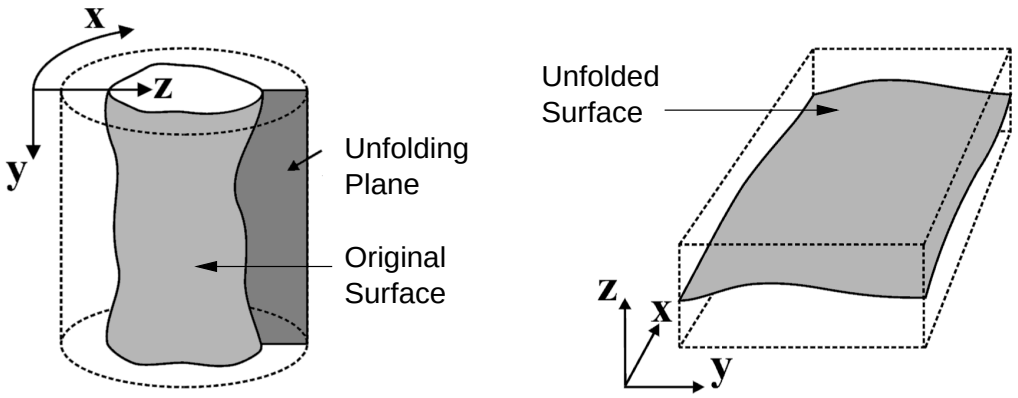

(b)

Fig. 3. (a) "Unfolding" an IVUS image frame using a polar transform; (b) this process is applied to the IVUS pullback, so that the detection of the cylindrical surfaces of varying radius is transformed to the detection of an elevation map of varying height.

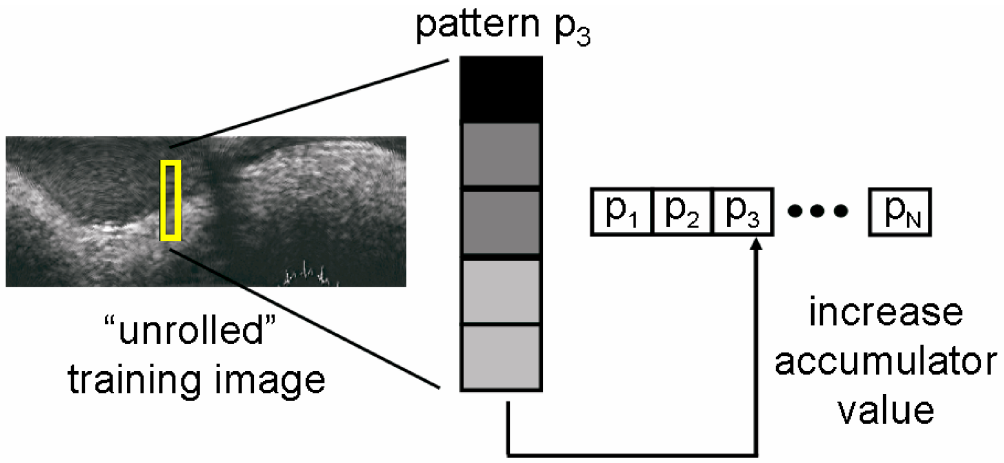

Fig. 4. Learned border patterns from a set of training images that have been segmented manually are examined: An accumulator represents a range of patterns; its entries corresponding to border patterns are increased with every incidence of that border pattern in the training set.

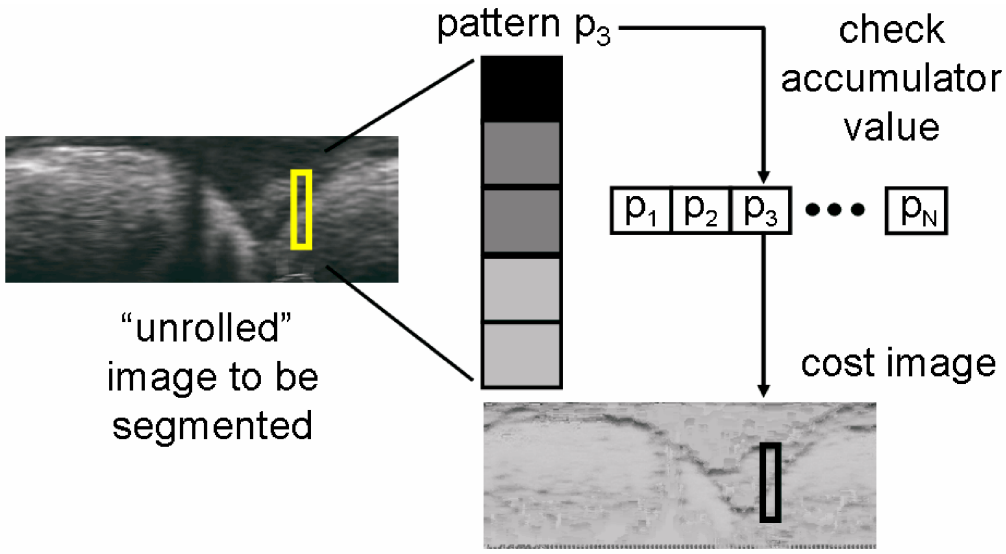

Fig. 5. Segmentation stage using the learned accumulator values of Fig. 4: The accumulator values are used to assign the likelihood of each pattern in the new image being a border pattern; the result is a cost image that contains the likelihood of each pixel being a border pixel.

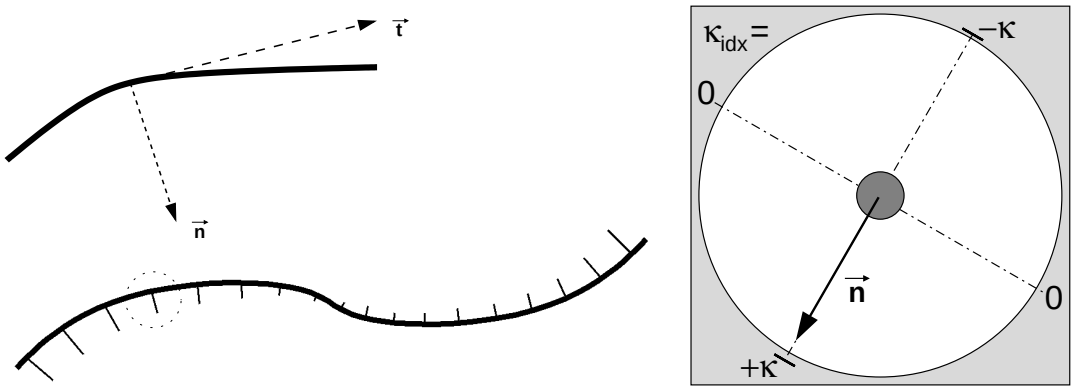

(a) (b)

Fig. 6. Definition of (a) normal and tangent vectors, (b) the circumferential curvature index κ_{idx} derived from the local curvature κ and the projected normal vector $\vec{n}$ for a specific IVUS frame; positive values indicate "inner" and negative values "outer" curvature.

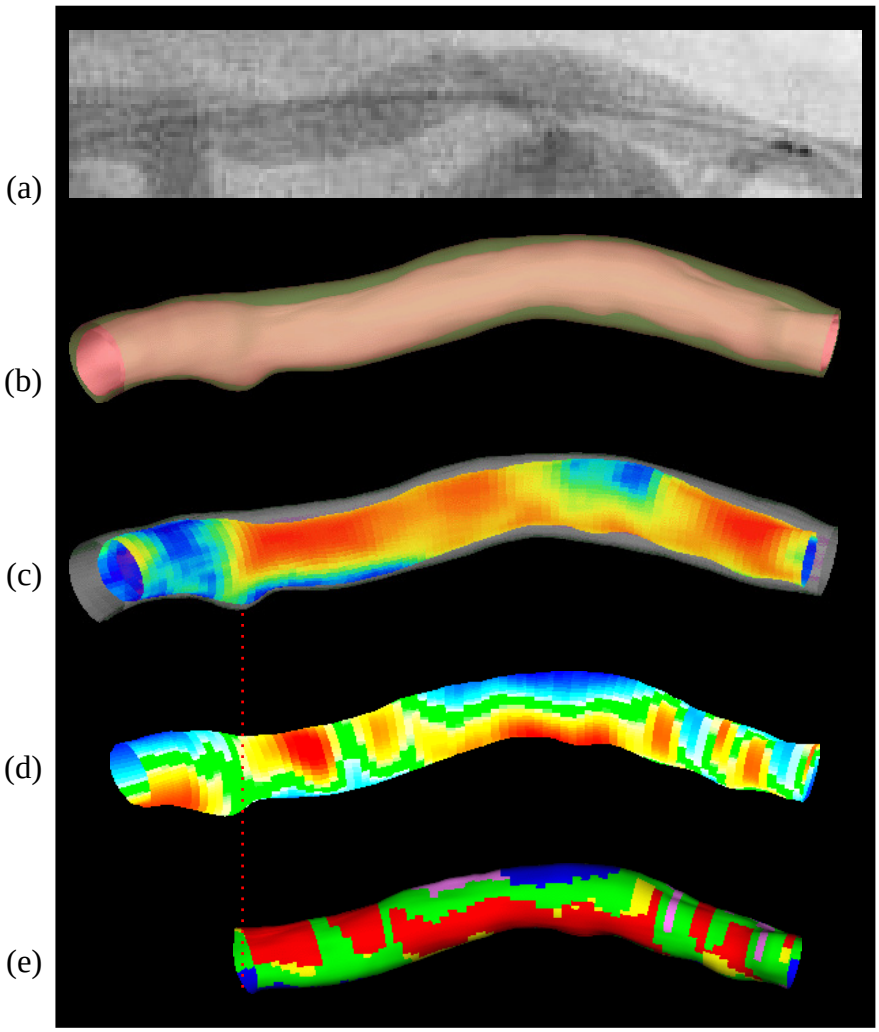

Fig. 7. Plaque thickness vs. curvature: (a) angiogram of a left anterior descending artery with the IVUS catheter inserted; (b) 3-D model with lumen and adventitia borders from fusion, where the volume between the red and green surfaces represents the vessel wall; (c) plaque-thickness annotation derived from the model shown in (b), where blue color indicates low and red color high wall thickness; (d) curvature-index annotation derived from (b), blue color marks "outer" and red "inner" curvature; (e) after classification into regions correlating the data from (c) and (d), with the branch segment removed from analysis as indicated by the red dotted line — see Section 2.6.1 for the definition of the regions.

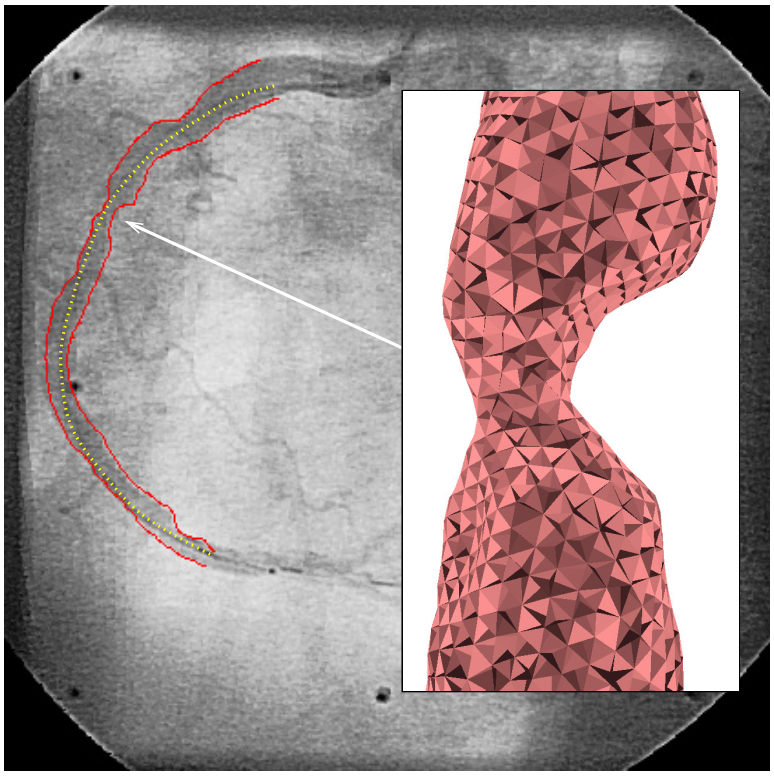

Fig. 8. One of the angiograms used for fusion, showing the IVUS catheter path (dotted line) and the lumen of a right coronary artery; the inset shows the corresponding tetrahedral mesh of the lumen at the stenotic vessel segment used for CFD analysis.

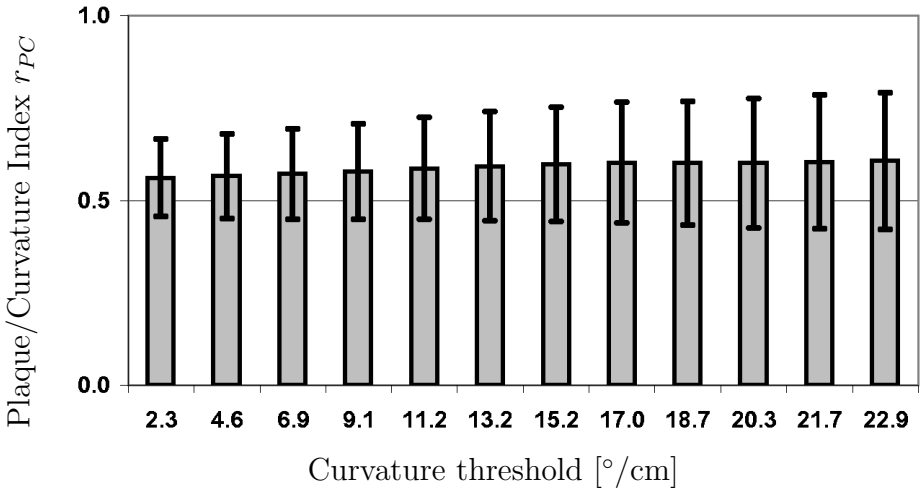

Fig. 9. Results from 60 analyzed vessels, analyzed as illustrated in Fig. 7, with means and standard deviations per curvature threshold; a value r_{PC}>0.5 indicates that our hypothesis was satisfied.

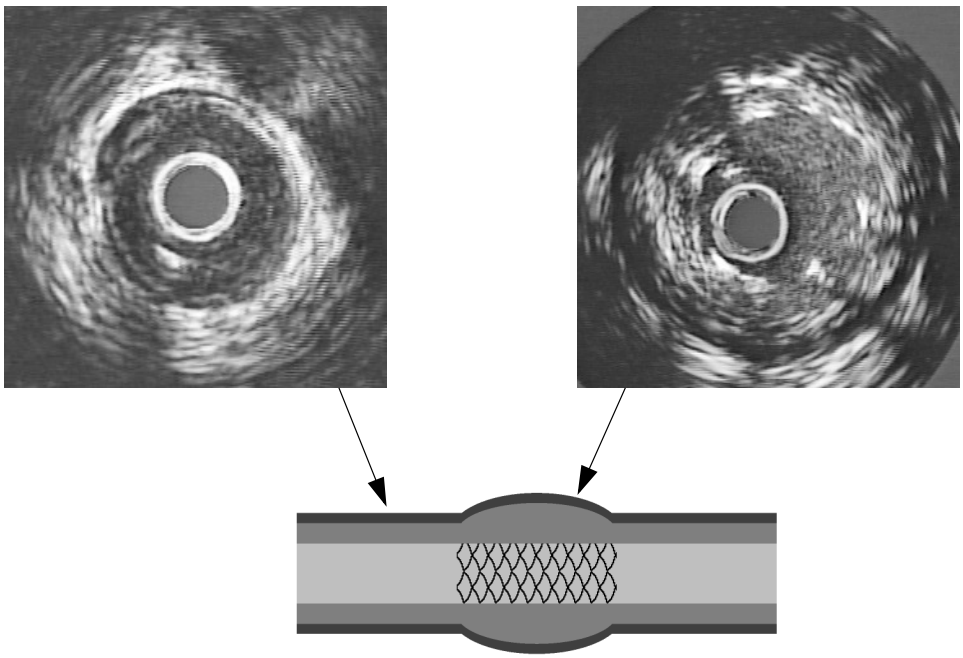

Fig. 10. IVUS frames of an untreated vessel segment with slight stenosis and after stent placement at a location with heavy disease.

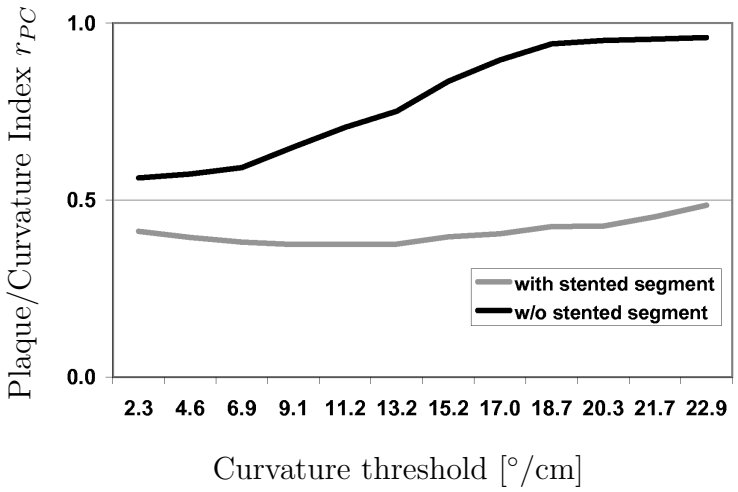

Fig. 11. Index r_{PC} for the vessel shown in Fig. 10 over the full vessel (gray) and with stented subsegments excluded (black); r_{PC}>0.5 is only satisfied after exclusion of the diseased segment as compared to the overall vessel.

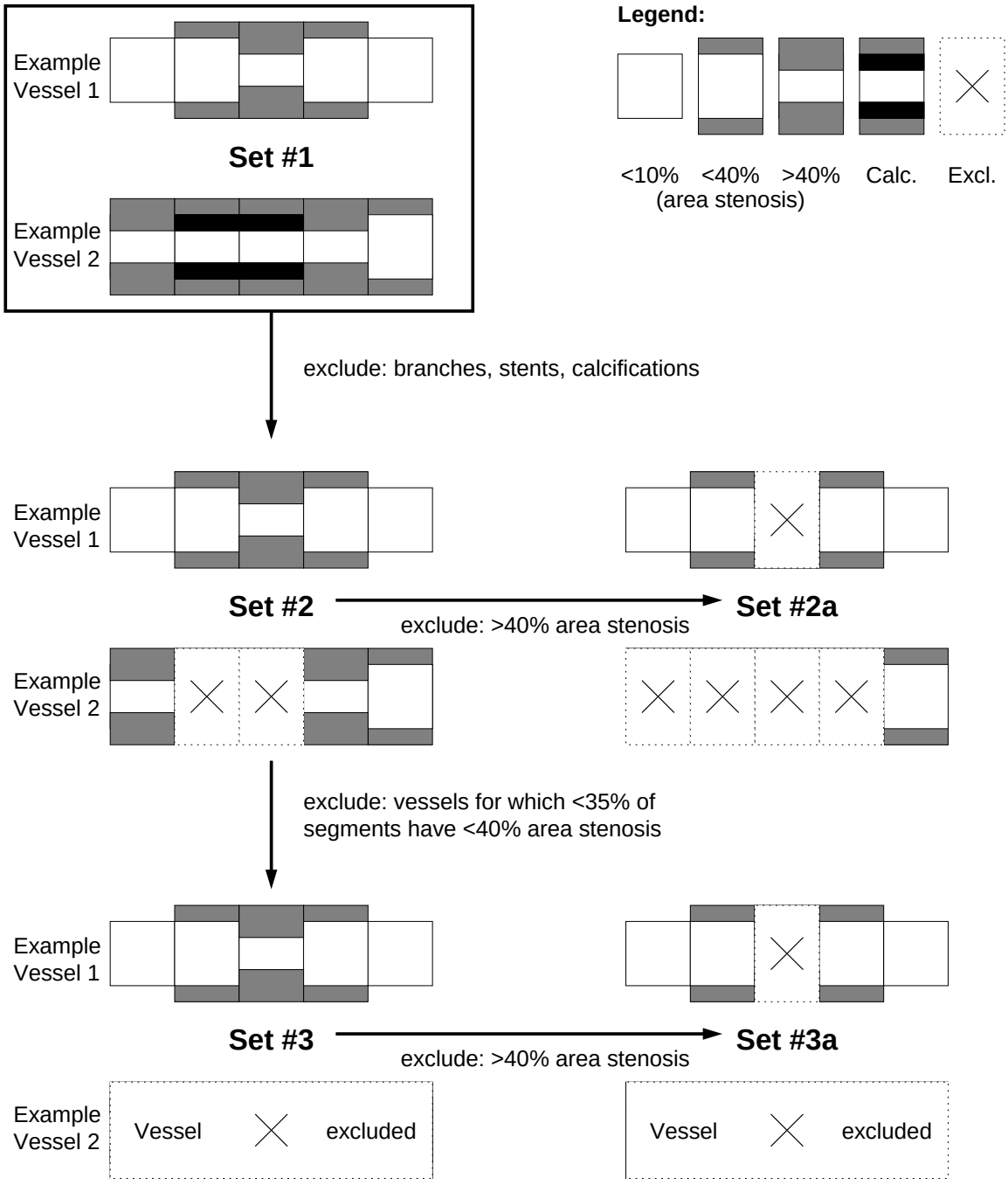

Fig. 12. Vessel and segment grouping for the definition of the sets described in 3.4.1, with two example vessels of different disease severity.